Earthq Eng & Eng Vib (2010) 9: 503-511 **DOI**: 10.1007/s11803-010-0032-2

Improvements of corner frequency and scaling factor for stochastic finite-fault modeling

Sun Xiaodan[1,2†], Tao Xiaxin[1‡] and Chen Fu[1§]

1. *School of Civil Engineering, Harbin Institute of Technology, Harbin 150090, China*

2. *School of Civil Engineering, Southwest Jiaotong University, Chengdu 610031, China*

Abstract: In this paper, three existing source spectral models for stochastic finite-fault modeling of ground motion were reviewed. These three models were used to calculate the far-field received energy at a site from a vertical fault and the mean spectral ratio over 15 stations of the Northridge earthquake, and then compared. From the comparison, a necessary measure was observed to maintain the far-field received energy independent of subfault size and avoid overestimation of the long-period spectral level. Two improvements were made to one of the three models (i.e., the model based on dynamic corner frequency) as follows: (i) a new method to compute the subfault corner frequency was proposed, where the subfault corner frequency is determined based on a basic value calculated from the total seismic moment of the entire fault and an increment depending on the seismic moment assigned to the subfault; and (ii) the difference of the radiation energy from each subfault was considered into the scaling factor. The improved model was also compared with the unimproved model through the far-field received energy and the mean spectral ratio. The comparison proves that the improved model allows the received energy to be more independent of subfault size than the unimproved model, and decreases the overestimation degree of the long-period spectral amplitude.

Keywords: stochastic finite-fault modeling; corner frequency; scaling factor; far-field received energy; long-period; spectral amplitude

1 Introduction

The stochastic finite-fault modeling technique has been developed to simulate ground motions near the epicenter of large earthquakes (Hartzell, 1978; Schneider *et al.*, 1993; Beresnev and Atkinson, 1997; Beresnev and Atkinson, 1998a; Silva *et al.*, 1999; Motazedian and Atkinson, 2005; Sun *et al.*, 2009). In the modeling, the fault is divided into several subfaults, where each subfault is considered to be a point source. The ground motion from a subfault is computed by a stochastic point-source approach. The ground motion from the entire fault is obtained by summing the contributions from all subfaults with time lags. In the stochastic point-source approach (Boore, 1983; 2003), the Fourier spectral acceleration at a site from a subfault is given by:

$$\mathrm{FA}(M_0, f, R) = S_a(M_0, f) \cdot G(R) \cdot D(R, f) \cdot A(f) \cdot P(f) \tag{1}$$

where $S_a(M_0,f)$ is the source spectrum, $G(R)$ accounts for the geometrical attenuation, $D(R,f)$ represents the energy dissipation attenuation, $A(f)$ describes the near-surface amplification by a transfer function of the regional crust velocity gradient, and $P(f)$ is a high-cut filter.

Correspondence to: Sun Xiaodan, School of Civil Engineering, Southwest Jiaotong University, 111–15 Beiyiduan, Erhuan Road, Chengdu 610031, China
Tel: +86-28-87634664
E-mail: vshermione@126.com
†Assistant Professor; ‡Professor; §Graduate

Supported by: National Natural Science Foundation of China Under Grant No. 50778058 and 90715038; National Key Technology R&D Program Under Contract No. 2006BAC13B02

Received May 15, 2009; **Accepted** August 18, 2010

2 Background

A widely used model for computing the source spectrum from a subfault was proposed by Beresnev and Atkinson (1998a) (denoted as the "BA model" in this paper). In this model, the assumption is that one subfault can cause N sub-events, where N is specified by:

$$N_{ij} = \frac{M_0}{m_0} \cdot \left(\frac{\overline{D}_{ij}}{\sum_{k=1}^{n_l} \sum_{l=1}^{n_w} \overline{D}_{kl}} \right) \tag{2}$$

Here, M_0 is the total seismic moment of the entire fault; m_0 is the seismic moment of the sub-event; $\overline{D}_{ij}$ is the slip on the subfault; n_l and n_w are the numbers of subfaults along the strike and dip directions, respectively. In the BA model, the acceleration source spectrum for each sub-event is given by:

$$S_a(f)=\frac{Cm_0(2\pi f)^2}{1+\left(f/f_c\right)^2} \tag{3}$$

where f_c is the corner frequency, as follows:

$$f_c=\frac{yz}{\pi}\cdot\frac{\beta}{\Delta l} \tag{4}$$

Here, β is the shear-wave velocity of the focal region; y ranges from 0.8 to 0.9, representing the ratio of the rupture velocity to β; and z is the radiation strength factor, usually taken as 1.68.

Some inaccuracies of the BA model were discussed by Beresnev and Atkinson (1998b) and Motazedian & Atkinson (2005):

(i) Assuming that a subfault causes many sub-events means that the subfault ruptures more than once. This assumption is physically impossible.

(ii) The simulated spectral level at high frequencies in the BA model depends on the subfault size. However, it should be independent of the fault discretization scheme.

(iii) The subfault corner frequency f_c in the BA model also depends on the subfault size. The larger the subfault size, the lower the corner frequency, which results in a greater low-frequency content in the simulated ground motion. Thus, to simulate the ground motions from large earthquakes which usually have rich low-frequency contents, the subfault size needs to be sufficiently large. A large subfault size, however, will lead to a rough description of the slip on the fault plane.

To address these limitations, Motazedian and Atkinson (2005) developed a source spectral model based on dynamic corner frequency, referred to as the "MA model" below. In this model, one subfault ruptures only once, and the acceleration source spectrum produced is formulated as:

$$S_{aij}(f)=\frac{CM_{0ij}H_{ij}(2\pi f)^2}{\left[1+\left(f/f_{cij}\right)^a\right]^b} \tag{5}$$

where H_{ij} is a scaling factor, and f_{cij} is the dynamic corner frequency depending on N_{Rij}, the cumulative number of subfaults ruptured by the time of the ijth subfault being triggered:

$$f_{cij}=4.9\times10^6\beta\left(\Delta\sigma/M_{0\text{ave}}\right)^{1/3}\cdot N_{Rij}{}^{-1/3} \tag{6}$$

As per Eq. (6), subfaults triggered early in the rupture process will have higher corner frequencies than those triggered later. This trend of corner frequency describes the fact that large amounts of energy are released at high frequencies when the rupture starts and shift toward low frequencies as the rupture develops (Motazedian and Atkinson, 2005). This trend, however, weakens the contribution of large-slip subfaults to the high-frequency energy (Sun *et al.*, 2009). Based on Masuda's model (1982), Sun *et al.* (2009) presented a source spectral model (referred to as the "Sun09 model") in which the subfault corner frequency is related to the slip distribution on the fault:

$$f_{cij}=4.9\times10^6\beta\left(\Delta\sigma/M_{0ij}\right)^{1/3}=4.9\times10^6\beta\left(\frac{\Delta\sigma}{M_0\cdot\overline{D}_{ij}\Big/\sum_{k=1}^{n_l}\sum_{l=1}^{n_w}\overline{D}_{kl}}\right)^{1/3} \tag{7}$$

For two subfaults with different slips, the subfault corner frequency will be different, and hence, the frequency content of the simulated seismic wave will be different. The acceleration source spectrum from the ijth subfault in the Sun09 model is defined by:

$$S_{aij}(f)=\frac{CM_{0ij}(2\pi f)^2}{\left[1+\left(f/f_{cij}\right)^a\right]^b} \tag{8}$$

where exponential coefficients a and b are determined by

$$\begin{cases}a=-0.375\lg A_{\text{Rup}}+1.81625\\ b=2/a\end{cases} \tag{9}$$

and where $A_{\text{Rup}}=N_{Rij}\cdot\Delta l\cdot\Delta w$ is the cumulative rupture area. The subfault corner frequency defined by Eq. (7) is adjusted by the cumulative rupture area A_{Rup} through coefficients a and b. For two subfaults with the same subfault moment, the one that ruptures later will have a lower corner frequency than the one that ruptures earlier. The Sun09 model was applied to the Northridge earthquake and the results showed that it can diminish the subfault size dependence in a similar manner as the MA model (Sun *et al.*, 2009).

3 Far-field received energy radiation

A good simulation approach should keep the simulated received energy independent of the fault discretization scheme because the total energy radiating from an earthquake is constant. Thus, the far-field received energies are calculated and compared by using the above three models. The example used in Motazedian and Atkinson (2005) (a vertical fault with a length of 40 km and a width of 20 km) was also employed herein. The fault depth range was 5–25 km, and the moment magnitude was 7.0. The slip distribution on the fault plane was assumed to be uniform. The observation point was 336 km away from the epicenter. With such an epicentral distance, the attenuation effects of all subfaults are almost the same (Motazedian and Atkinson, 2005). Simulations were performed for different subfault

sizes, including 1, 2, 5 and 10 km. The far-field received energy from the whole fault is the superposition of the contributions from all subfaults, and the far-field received energy from each subfault is proportional to the square of the Fourier velocity spectrum. All the assumed input parameters for the simulation are listed in Table 1 (see Motazedian and Atkinson (2005) for details). With the same input parameters, the far-field received energies for different subfault sizes were derived based on the BA, MA and Sun09 models separately and are presented in Fig. 1. Similar as the results in Motazedian and Atkinson (2005), the received energy by using the MA model is almost identical for different subfault sizes, whereas the magnitude of energy and the gap of its overlap by using the BA and Sun09 models vary significantly depending on the subfault size. Obviously, the Sun09 model does not remove the subfault size dependence from the simulated energy.

Table 1 Simulation parameters

$Q(f)$	$333f^{0.74}$
Distance dependence duration	T_0+0.1R
Geometric spreading	$1/R$ (R≤70 km)
	$1/R^0$ (70 km<R<130 km)
	$1/R^{0.5}$ (R≥130 km)
Kappa	0.03
Pulsing percentage	50%
Crustal shear-wave velocity	3.7 km/s
Crustal density	2.8 g/cm^3
Radiation strength factor	1.6
Stress drop	5×10^6 Pa

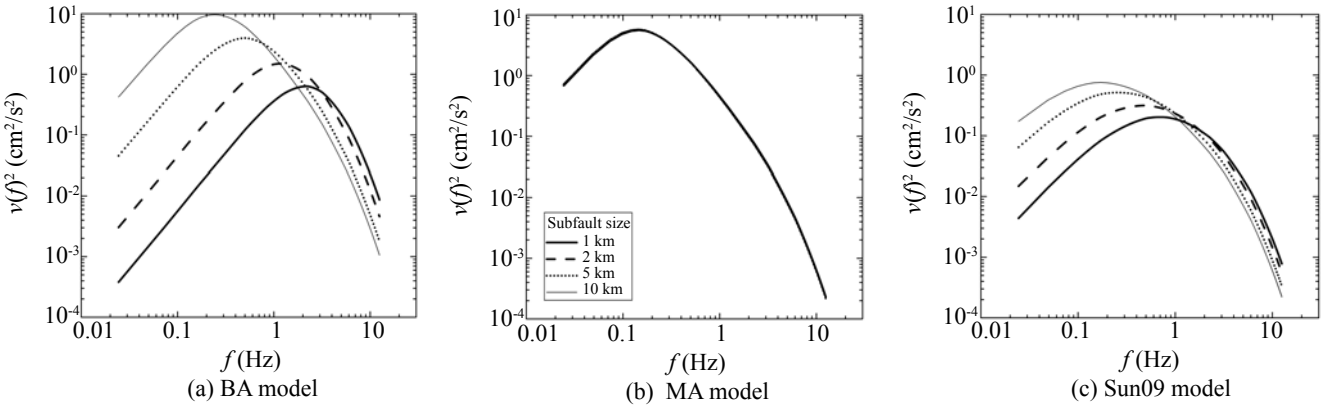

(a) BA model (b) MA model (c) Sun09 model

Fig. 1 Comparison of far-field received energies vs frequency for different subfault sizes

This failure motivated the authors to determine the reason for the success of the MA model in both simulated energy and simulated ground motion. The investigation is started from the corner frequency of the velocity spectrum of a single subfault, since each energy curve in Fig. 1 is the contribution of the velocity spectra from all subfaults. Table 2 shows the subfault corner frequencies by using the BA and Sun09 models (Eq. 4 and Eq. 7), which are apparently different for different subfault sizes. Accordingly, the velocity spectrum of the subfault and the superposed velocity spectrum of all subfaults will reach their peaks at different frequencies for different subfault sizes. By contrast, the MA model cannot give all subfaults a definite corner frequency for a definite subfault size due to the $N_{\mathrm{R}ij}$ in the dynamic corner frequency concept, so statistical analysis is performed on the subfault corner frequencies to observe the general level. Figure 2 shows the percentage histograms of the subfault corner frequencies by using the MA model, arranged in order of subfault sizes of 1, 2, 5 and 10 km from left to right. One may observe that, for all four subfault size cases, the majority (nearly over 90%) of subfaults have a corner frequency lower than 0.2 Hz. Accordingly, the velocity spectrum of the subfault and the superposed velocity spectrum of all subfaults will reach their peaks at about the same level of the frequency for different subfault sizes.

In addition to the dynamic corner frequency concept, the scaling factor H_{ij} in Eq. (5) is also indispensable for the successful conservation of the simulated energy. Figure 3 shows the simulated received energy by using the MA model without H_{ij}. Note that the shape of the

Table 2 Subfault corner frequencies Hz

Model	Subfault sizes			
	1 km	2 km	5 km	10 km
BA model	1.5	0.75	0.3	0.15
Sun09 model	0.88	0.55	0.3	0.19

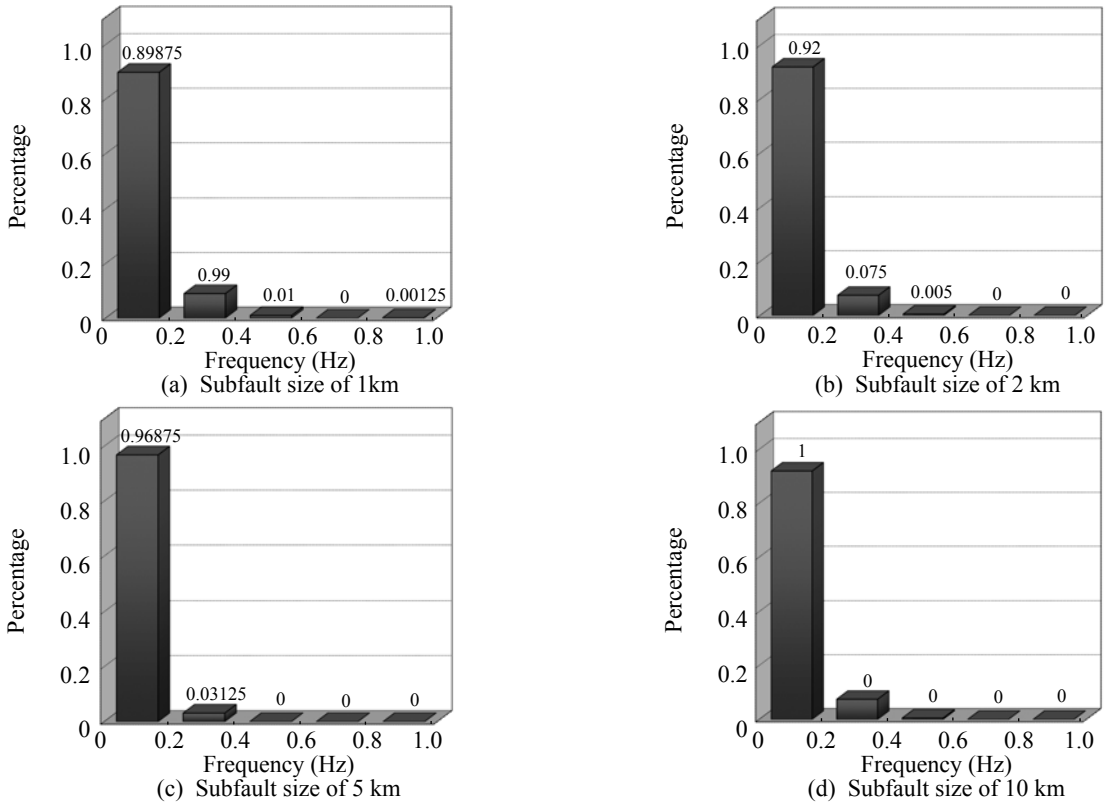

Fig. 2 Histograms of the subfault corner frequencies by using the MA model

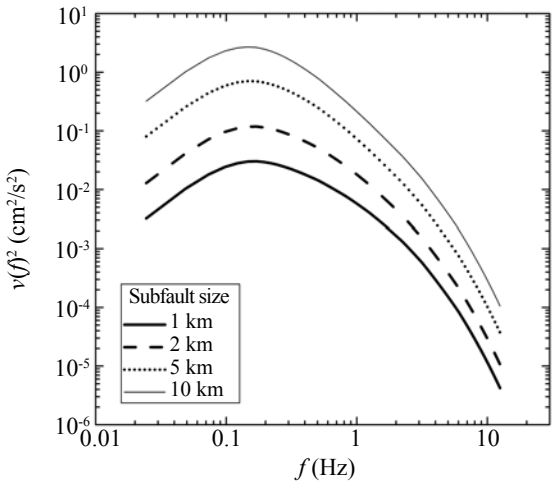

Fig. 3 Far-field received energies by using the MA model without H_{ij}

energy spectrum is very similar for different cases due to the dynamic corner frequency concept, while a large diminishing effect on the spectrum amplitude is apparent. The scaling factor H_{ij} is a frequency-independent parameter developed to minimize this diminishing effect (Motazedian and Atkinson, 2005).

Thus far, the success of the MA model to enable the simulated energy to be independent of the subfault size is attributed to two factors: the dynamic corner frequency concept, which keeps the shape of the received energy spectrum; and the scaling factor H_{ij}, which balances the decrease of the spectral amplitude.

4 Long-period spectral level

In this section, the 1994 Northridge earthquake was adopted to investigate the simulation accuracy of the MA model. Figure 4 shows the slip on the fault of the Northridge earthquake from inversion (Wald *et al*., 1996), and Fig. 5 shows a discretized model of the fault with a subfault size of 3 km (Tao and Anderson, 2002). A summary of the simulation parameters is listed in Table 3 (see Beresnev and Atkinson, 1998a for details). Particularly, the stress drop of 60 bars and the pulsing area percentage of 25% were suggested by Motazedian and Atkinson (2005) for California earthquakes after a wide range of calibrations. Ground motions at 15 rock stations that recorded the Northridge earthquake were synthesized. The names and geographies of the 15 rock stations are listed in Table 4 (NGA database, 2006). The 15 stations surround the fault at different azimuths, so the synthesis can include coverage of the directivity effects.

For each site, the simulation was performed 30 times with different random phase series in order to ignore the effect of the variation of phase series on the results (Beresnev and Atkinson, 1998a; Tao *et al.*, 2009); PSAs from the 30 realizations were computed, where a PSA is the 5% damped acceleration response spectrum; the amplitude ratio of the average PSA of the 30 realizations to the PSA from the record was then calculated at each period. The mean spectral ratio over the 15 stations is shown in Fig. 6, together with the standard deviations (dash lines) and the 95% confidence intervals of the

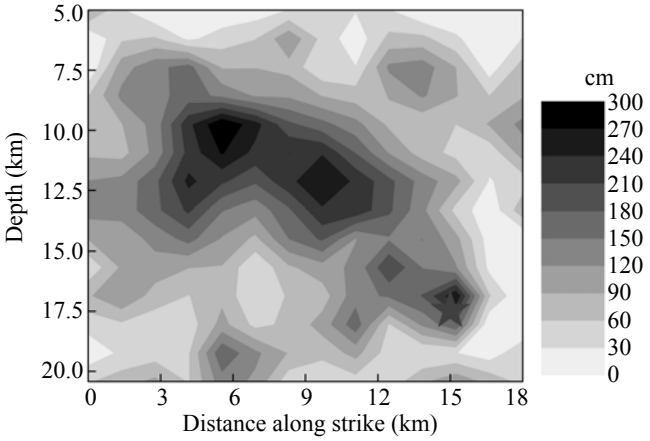

Fig. 4 Slip on the fault for the Northridge earthquake (Wald *et al*., 1996)

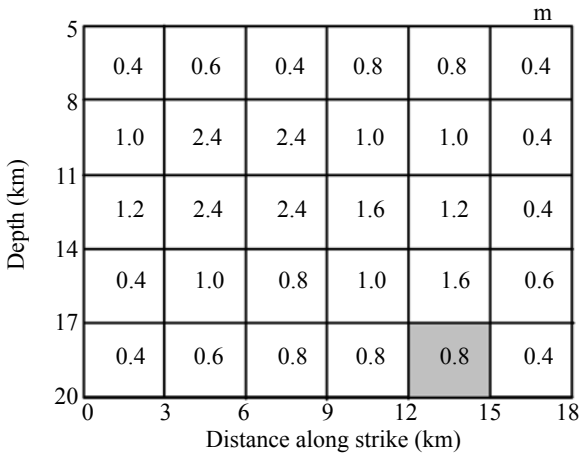

Fig. 5 Discretized finite-fault model

Table 3 Simulation parameters

Fault orientation	strike 122 ° , dip 40 °
Fault depth	5 km
Moment magnitude	6.7
$Q(f)$	$150f^{0.5}$
Windowing function	Saragoni-Hart
Kappa	0.04
Crustal shear-wave velocity	3.7 km/s
Crustal density	2.8 g/cm^3
Stress drop	6×10^6Pa
Distance dependence duration	T_0+0.1R
Pulsing area percentage	25%
Geometric spreading	$1/R$ ($R\leq$70 km)
	$1/R^0$ (70 km<R<130 km)
	$1/R^{0.5}$ ($R\geq$130 km)
Local amplification	Boore-Joyner (1997) western North America generic rock site

mean derived from the student distribution (the hatched bands). One can observe an underestimation at short periods (<1 s) and an apparent overestimation at long periods, which increases as the period increases. According to Motazedian and Atkinson (2005), the amplitudes at long periods decrease by reducing the pulsing area percentage. In this case, the minimum pulsing area percentage is about 3.33% because the pulsing length should not be less than the subfault length. The simulation was performed again with the minimum pulsing area percentage, and the obtained mean spectral ratio is shown in Fig. 7. Unexpectedly, the overestimation at long periods in Fig. 6 still exists in Fig. 7, as if the pulsing area percentage was not used. The simulation was also performed based on another discretized fault model suggested by Beresnev and Atkinson (1998a), and the obtained mean spectral ratio, as illustrated in Fig. 8, shows a very similar trend at long periods as those in Figs. 6 and 7.

Table 4 Rock stations

Station name	Latitude	Longitude	Location	Hypocentral distance (km)	Agency
ANB	34.758	-118.361	Antelope Buttes	66.31	CDMG
BCY	34.204	-118.302	Burbank - Howard Rd.	29.05	USC
GPK	34.118	-118.299	LA - Griffith Park Observatory	30.86	USGS
L09	34.608	-118.558	Lake Hughes #9	48.07	CDMG
L4B	34.650	-118.477	Lake Hughes #4B - Camp Mend	52.92	CDMG
LPK	34.109	-119.065	Point Mugu - Laguna Peak	51.35	CDMG
LV3	34.596	-118.243	Leona Valley #3	54.84	CDMG
LWE	34.114	-118.380	LA - Wonderland Ave	25.82	USC
LWS	34.089	-118.435	LA - N Faring Rd	24.39	USC
MCN	34.078	-118.694	Monte Nido Fire Station	25.97	USGS
MSM	34.086	-118.481	LA - Chalon Rd	22.99	USC
ORR	34.564	-118.642	Castaic - Old Ridge Route	44.29	CDMG
PCD	34.334	-118.396	Pacoima Dam (downstr)	26.85	CDMG
PKC	34.296	-118.375	Pacoima Kagel Canyon	26.04	CDMG
SSA	34.232	-118.710	Santa Susana Ground	22.83	USGS

Note: CDMG: California Division of Mines and Geology; USC: University of Southern California; USGS: United States Geological Survey

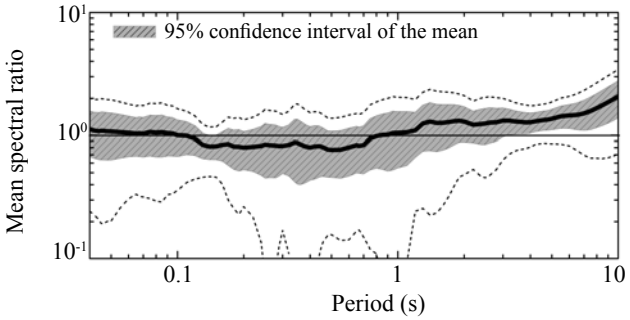

Fig. 6 Mean spectral ratio by using the MA model

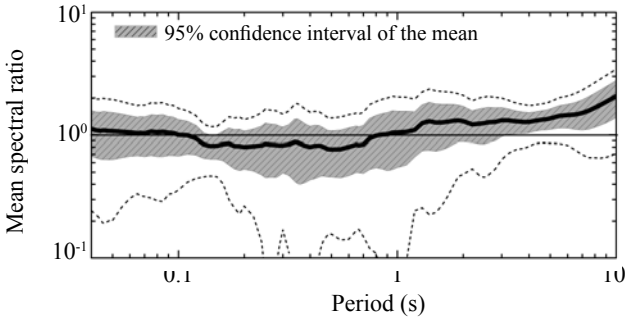

Fig. 7 Mean spectral ratio, for the pulsing area percentage of 3.33%

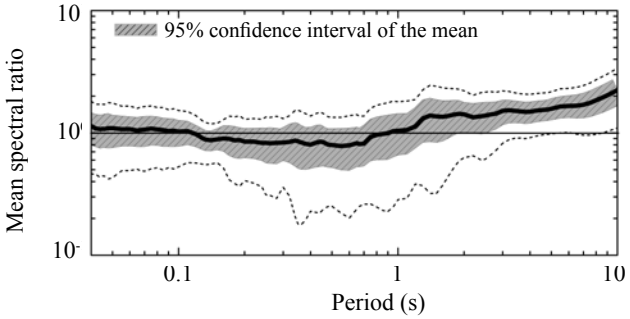

Fig. 8 Mean spectral ratio, from the discretized fault model suggested by Beresnev and Atkinson (1998)

The above investigation indicates that the overestimation on the long-period spectral level does not result from the selected discretized fault model and cannot be balanced by adjusting the pulsing area percentage. In our opinion, this overestimation at long periods results from the low general level of subfault corner frequency generated due to the creative dynamic corner frequency concept. The subfault corner frequency controls the shape of the energy spectrum, i.e., decides the distribution of the energy in the entire frequency range. When the total amount of radiated energies is constant, a low subfault corner frequency will mean that most of the radiated energies are distributed in low frequencies. Therefore, an effective way to balance the overestimation on the long-period spectral level is by considering a new concept to give a reasonable level to the subfault corner frequency so that some radiated energies can be shifted toward high frequencies.

5 Improvements

In the subsections below, two improvements are made on the MA model, including a new concept of subfault corner frequency and a modification to the determination of the scaling factor H_{ij}.

5.1 Corner frequency

In the new concept, the subfault corner frequency is determined based on a basic value added to an increment, as given by

$$f_{cij} = f_0 \left[1 + \left(\frac{M_{0ij}}{M_{0\text{ave}}} \right)^{1/3} \right] \tag{10}$$

where $M_{0\text{ave}} = M_0 / N$ is the average moment, and M_{0ij} is the subfault moment as defined in Eq. (7). The basic corner frequency, f_0, is decided by the original definition of the corner frequency (Boore, 2003):

$$f_0 = 4.9 \times 10^6 \beta \left(\Delta\sigma / M_0 \right)^{1/3} \tag{11}$$

Equation (11) well represents the inverse proportional relationship between the seismic moment and the corner frequency, which is observed in most earthquakes; thus, it is reasonable to use Eq. (11) to define the general level of subfault corner frequencies and to control the shape of the simulated ground motion spectrum. The increment of the corner frequency is related to the ratio of the subfault moment to the average moment so that the simulated seismic wave from large-slip subfaults will have greater high-frequency content than smaller-slip subfaults. Considering that seismic moment is inversely proportional to the cube of corner frequency, the increment is assumed to be on the order of 1/3 the power of the moment ratio.

In other words, in the new concept, all subfaults have a common basic value for corner frequency, and the corner frequency of each subfault is obtained by adjusting the basic value based on the subfault moment. The common basic value ensures that the general level of subfault corner frequencies will be independent of the fault discretization scheme. This basic value is equal to the minimum corner frequency defined in the dynamic corner frequency concept. Therefore, the general levels of subfault corner frequencies by the two concepts are very similar. By adding the increment, however, the corner frequency for most subfaults by the new concept will be higher than by the dynamic corner frequency concept, and hence, the working level of the subfault corner frequencies will also be higher. This enhancement of the corner frequency level implies that the energy spectrum curve will reach its peak at a higher frequency and that some of the energies will be accordingly shifted away from low frequencies.

5.2 Scaling factor

The scaling factor H_{ij} in the MA model is deduced based on an assumption that the high-frequency radiated energy for all subfaults is equal to the average energy (Motazedian and Atkinson, 2005):

$$E_{ij} = E / N \tag{12}$$

where E is the total energy radiating from the entire fault. However, the high-frequency energies radiating from different parts of the fault are different. In addition to the rupture starting point, the large-slip areas are also the areas that reproduce rich high-frequency seismic waves (Miyake *et al.*, 2003). By this assumption, the contributions of large-slip subfaults to the simulated high-frequency energy are weakened. On the other hand, Eq. (13), which Motazedian and Atkinson (2005) used to compute E, was originally developed for a point source (Vassiliou and Kanamori, 1982; Venkataraman *et al.*, 2002):

$$E = \int \left\{ CM_0 (2\pi f) \Big/ \left[1 + \left(f / f_0 \right)^2 \right] \right\}^2 \mathrm{d}f \tag{13}$$

It is inappropriate to simplify the entire fault into a point source to compute the energy. In finite-fault modeling, the discretized subfault is considered as a point source; therefore, Eq. (13) should be used only for subfaults.

In our improvement, the scaling factor is deduced from

$$E_{ij} = E_{ij}^* \tag{14}$$

where E_{ij} is the high-frequency energy radiating from the ijth subfault based on Eq. (5) and Eq. (13):

$$E_{ij} = \int \left\{ \frac{CM_{0ij} H_{ij} (2\pi f)}{1 + \left(f / f_{cij} \right)^2} \right\}^2 \mathrm{d}f \tag{15}$$

E^*_{ij} is the high-frequency energy radiated from a separate point source with the same moment as the ijth subfault:

$$E_{ij}^* = \int \left\{ \frac{CM_{0ij} (2\pi f)}{1 + \left(f / f_{0ij} \right)^2} \right\}^2 \mathrm{d}f \tag{16}$$

In which $f_{0ij} = 4.9 \times 10^6 \beta \left(\Delta\sigma / M_{0ij} \right)^{1/3}$. Note that the f_{0ij} in Eq. (16) is different from f_{cij} in Eq. (15). f_{cij} is defined from the entire fault's point of view. It controls the shape of the simulated spectrum, and represents the corner frequency that an earthquake with a moment of M_0 should have. The f_{0ij}, by contrast, is defined from the point of view of the subfault. It represents the corner frequency that a separate point source with a moment of M_{0ij} should have. Equation (14) indicates that the radiation energy obtained by considering the subfault as a part of the entire fault should be equal to that obtained by considering the subfault as a separate point source. Following Eqs. (14), (15) and (16) above, the scaling factor is redefined as:

$$H_{ij} = \sqrt{\frac{\int \left\{ f \Big/ \left[1 + \left(f / f_{0ij} \right)^2 \right] \right\}^2 \mathrm{d}f}{\int \left\{ f \Big/ \left[1 + \left(f / f_{cij} \right)^2 \right] \right\}^2 \mathrm{d}f}} \tag{17}$$

Rewriting Eq. (15) into discretized form gives:

$$H_{ij} = \sqrt{\frac{\sum \left\{ f \Big/ \left[1 + \left(f / f_{0ij} \right)^2 \right] \right\}^2}{\sum \left\{ f \Big/ \left[1 + \left(f / f_{cij} \right)^2 \right] \right\}^2}} \tag{18}$$

6 Verification

In this section, the case in Section 2 is used again to test the effect of the improvements. Considering that both the corner frequency and scaling factor in our improvement are slip-dependent, the slip distribution on the fault plane in this case is changed to be non-uniform. For comparison, the MA model is also applied, and the results are shown in Fig. 9. Note that in nearly the entire frequency range, the MA model no longer performs as

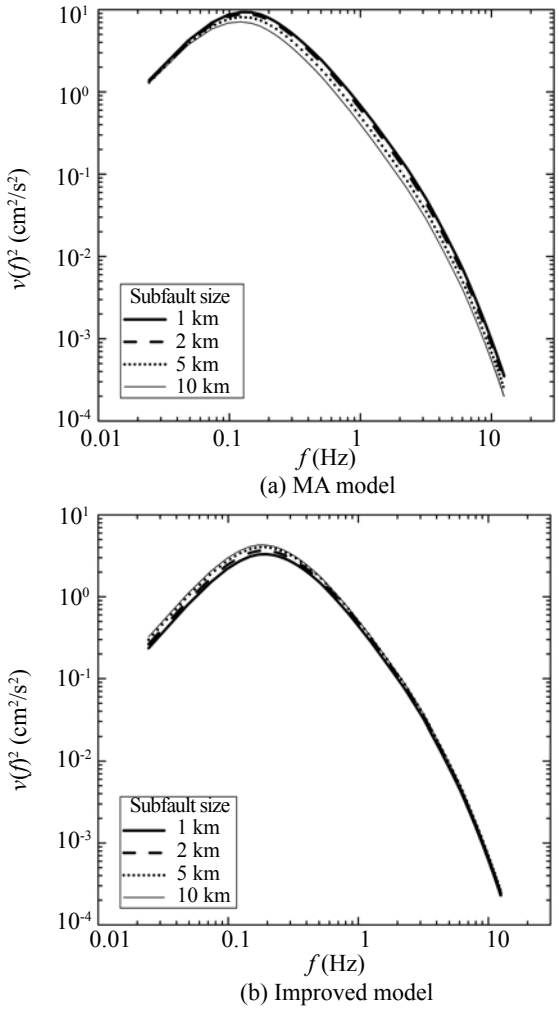

Fig. 9 Far-field received energy for different subfault sizes

perfectly as it did in the case of uniform slip distribution (Fig. 1(b)). The improved model, by contrast, obtains greater accuracy, especially in the high frequency range (>1 Hz) where the stochastic approach is expected to perform well.

Figure 9 also shows that the peak of the energy curve moves towards the right after the improvements. This means that part of the energy shifts towards higher frequencies; the low-frequency spectral level may decrease accordingly. Figure 10 shows the mean spectral ratio over 15 stations by using the improved model. Comparing Fig. 10 with Fig. 6, the overestimation at

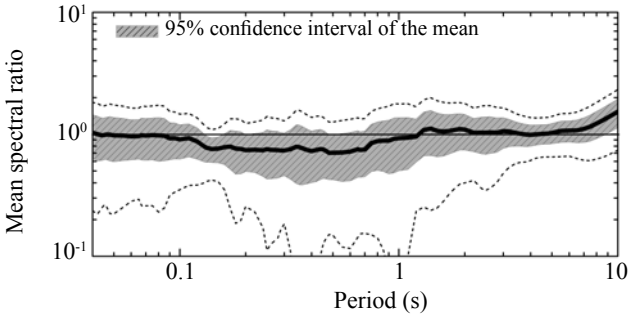

Fig. 10 Mean spectral ratio obtained by using the improved model

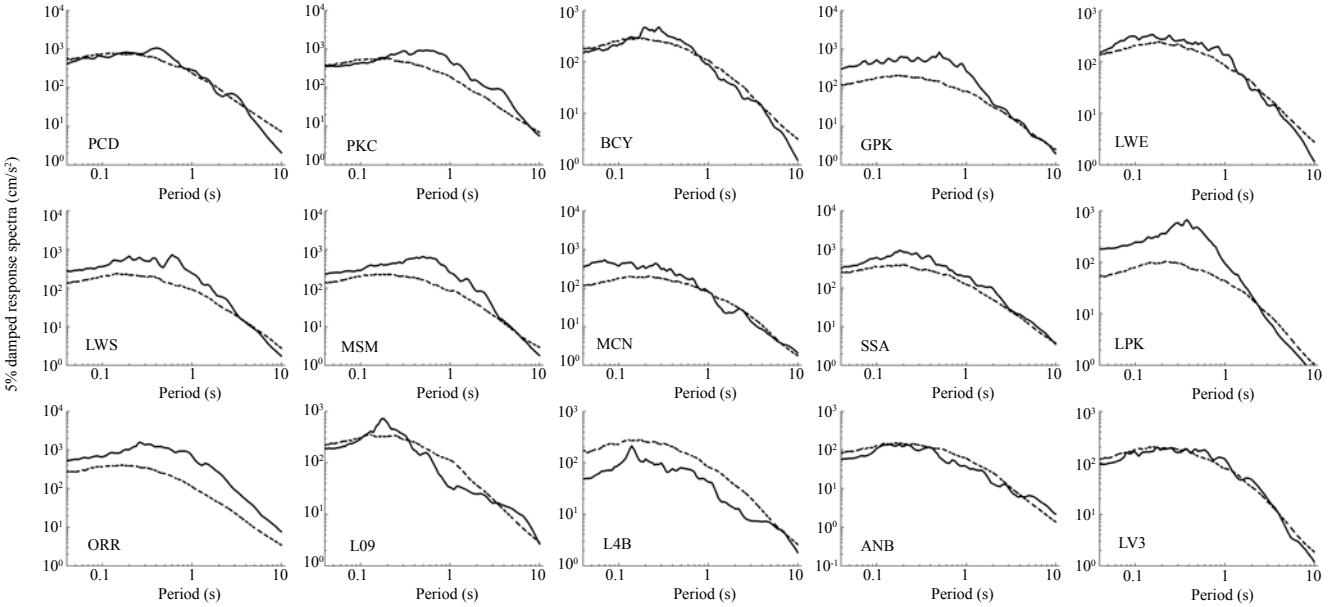

Fig. 11 PSAs from the synthesized accelerograms (dash line) and records (solid line)

long periods is markedly suppressed. The simulated and recorded PSAs at the 15 stations are shown in Fig. 11, in which good agreement can be observed at most stations, especially at stations PCD, BCY, LWE, ANB and LV3. Large discrepancies in periods of less than about 1 sec exist at some stations (GPK, LPK and ORR), but these should be attributed to the incapability of the stochastic technique to account for the effects of local response, topography or basin geometry (Beresnev and Atkinson, 1998a).

7 Conclusions and discussions

In this paper, two improvements on the source spectral model in stochastic finite-fault modeling were presented: a new concept of subfault corner frequency and a scaling factor modification. In the new concept of subfault corner frequency, a basic corner frequency is defined to ensure that the simulated received energy is independent of the fault discretization scheme. The non-uniform slip distribution was considered in the concept of the subfault corner frequency and the modification of the scaling factor, which covers the concept shortage of the BA and MA approaches in describing the non-uniform radiation of seismic energy.

The case study on far-field received energy shows that in the high frequency range (>1 Hz), the use of the improved model yields a better conservation of the far-field received energy than the MA model, especially for faults with non-uniform slip distribution. Applications to the Northridge earthquake showed that the improvements can effectively decrease the overestimation degree of the spectral level at long periods. In addition, the improved model yielded satisfactory simulated PSAs at most of the 15 stations. Although a few discrepancies exist at certain stations and frequencies, these resulted from natural defects in the stochastic technique.

In this paper, the software computer programs FINSIM and EXSIM (2005 version) were used to run the stochastic approaches based on the BA and MA models, separately. Some research was aimed at improving the EXSIM. Motazedian (2009) proposed to introduce a coefficient to control the low-frequency

amplitude, which is arbitrarily determined by users. In our opinion, however, as the pulsing area percentage in EXSIM is already a user free-input parameter to control the low-frequency amplitude, and it may be not necessary to introduce another free-input parameter for the same purpose.

Acknowledgement

The authors sincerely appreciate Dr. Dariush Motazedian and Dr. Igor Beresnev for their generosity in sharing the codes. Discussions with them during the research reported in this paper also significantly benefited the authors. Excellent assistance on the use of English grammar from Dr. Hoboo Ha, Professor Kexu Zhang, and Dr. Dariush Motazdian is also appreciated. Special thank is also given to Ms. Xiaoying Sun for her big helps on collecting earthquake data and on editing the manuscript.

References

Beresnev IA and Atkinson G (1997), "Modeling Finite-Fault Radiation from the ω^n Spectrum," *Bull Seism Soc Amer*, **87**(1): 67−84.

Beresnev IA and Atkinson G (1998a), "Stochastic Finite-fault Modeling of Ground Motions from the 1994 Northridge, California, Earthquake (I): Validation on Rock Sites," *Bull Seism Soc Amer*, **88**(6): 1392−1401.

Beresnev IA and Atkinson G (1998b), "Finsim—a Fortran Program for Simulating Stochastic Acceleration Time Histories from Finite Faults," *Seism. Res. Lett.*, **69**(1): 27−32.

Boore DM (1983), "Stochastic Simulation of High-frequency Ground Motions Based on Seismological Models of the Radiated Spectra," *Bull. Seism. Soc. Am.*, **73**: 1865–1894.

Boore DM (2003), "Simulation of Ground Motion Using the Stochastic Method," *Pure and Applied Geophysics*, **160**: 635–676.

Boore DM and Joyner WB (1997), "Site Amplifications for Generic Rock Sites," *Bull. Seism. Soc. Am*, **87**: 327–341.

Hartzell S (1978), "Earthquake Aftershocks as Green's Functions," *Geophys. Res. Lett.*, **5**: 1–14.

Masuda T (1982), "Scaling Relations for Source Parameters of Micro-earthquakes in the Northeastern Part of Japan," *Doctorial Dissertation*, Tohoku University.

Miyake H, Iwata T and Irikura K (2003), "Source Characterization for Broadband Ground-motion Simulation: Kinematic Heterogeneous Source Model and Strong Motion Generation Area," *Bull. Seism. Soc. Am.*, **93**(6): 2531–2545.

Motazedian D (2009), EXSIM_Bata. http://http-server.carleton.ca/~dariush/research/EXSIM_Beta.zip. NGA_flatfile (2006), http://peer.berkeley.edu/products/nga_flatfiles_dev.html.

Motazedian D and Atkinson GM (2005), "Stochastic Finite-fault Modeling Based on a Dynamic Corner Frequency," *Bull. Seism. Soc. Am.*, **95**(3): 995–1010.

Schneider J, Silva W, and Stark C (1993), "Ground Motion Model for the 1989 *M* 6.9 Loma Prieta Earthquake Including Effects of Source, Path and Site," *Earthquake Spectra*, **9**: 251–287.

Silver W, Gregor N and Darragh B (1999), "Near Fault Ground Motions," *A Pearl Report of PG&E/CEC/Caltrans*.

Sun XD, Tao XX, Wang GX and Liu TJ (2009), "Dynamic Corner Frequency in Source Spectral Model for Stochastic Synthesis of Ground Motion," *Earthquake Science*, **22**(3): 271–276.

Tao XX and Anderson JG (2002), "Near Field Strong Ground Motion Simulation," *Paper Presented at the Proceeding of ICANCEER*, Harbin.

Tao XX, Sun XD, Liu HM, Li P (2009), "Some Issues on Forecast of Strong Ground Motion Field," *The 7th International Conference on Earthquake Resistant Engineering Structures*, Cyprus.

Vassiliou MS and Kanamori H (1982), "The Energy Release in Earthquakes," *Bull. Seism. Soc. Am.*, **72**(2): 371–387.

Venkataraman A, Rivera L and Kanamori H (2002), "Radiated Energy from the 16 October 1999 Hector Mine Earthquake: Regional and Teleseismic Estimates," *Bull. Seism. Soc. Am.*, **92**(4): 1256–1265.

Wald DJ, Heaton TH and Hudnut KW (1996), "The Slip History of the 1994 Northridge, California Earthquake Determined from Strong Motion, Teleseismic, GPS, and Leveling Data," *Bull. Seism. Soc. Am.*, **86**: S49–S70.